Clim Dyn
DOI 10.1007/s00382-014-2153-1

On the stability of the Atlantic meridional overturning circulation during the last deglaciation

Wei Liu · Zhengyu Liu · Jun Cheng · Haibo Hu

Received: 4 October 2013 / Accepted: 17 April 2014
© Springer-Verlag Berlin Heidelberg 2014

Abstract Using a generalized stability indicator L, we explore the stability of the Atlantic meridional overturning circulation (AMOC) during the last deglaciation based on a paleoclimate simulation. From the last glacial maximum, as forced by various external climate forcings, notably the meltwater forcing, the AMOC experiences a collapse and a subsequent rapid recovery in the early stage of deglaciation. This change of the AMOC induces an anomalous freshwater divergence and later convergence across the Atlantic and therefore leads to a positive L, suggesting a negative basin-scale salinity advection feedback and, in turn, a mono-stable deglacial AMOC. Further analyses show that most anomalous freshwater is induced by the AMOC via the southern boundary of the Atlantic at 34°S where the freshwater transport (M_{ovS}) is about equally controlled by the upper branch of the AMOC and the upper ocean salinity along 34°S. From 19 to 17 ka, as a result of multiple climate feedbacks associated with the AMOC change, the upper ocean at 34°S is largely salinified, which helps to induce a switch in M_{ovS}, from import to export. Our study has important implications to the deglacial simulations by climate models. A decomposition of L shows that the AMOC stability is mostly determined by two terms, the salinity stratification at 34°S and the change of stratification with the AMOC. Both terms appear positive in model. However, the former is likely to be distorted towards positive, as associated with a common bias existing over the South Atlantic in climate models. Therefore, the AMOC is potentially biased towards mono-stability in most paleoclimate simulations.

Keywords AMOC · Stability indicator · Freshwater transport · Feedback · The last deglaciation

W. Liu
Cooperative Institute for Climate and Satellites, North Carolina State University, Raleigh, NC, USA

W. Liu
NOAA National Climatic Data Center, Asheville, NC, USA

W. Liu (✉)
CASPO, Scripps Institution of Oceanography, University of California, San Diego, La Jolla, CA, USA
e-mail: wliu5wisc@gmail.com

Z. Liu
Lab. Climate, Ocean and Atmosphere Studies, Peking University, Beijing, China

Z. Liu
Center for Climatic Research, University of Wisconsin-Madison, Madison, WI, USA

J. Cheng
Key Laboratory of Meteorological Disaster of Ministry of Education, School of Marine Sciences, Nanjing University of Information Science and Technology, Nanjing, China

H. Hu
School of Atmospheric Sciences, Nanjing University, Nanjing, China

1 Introduction

Since the last glacial maximum (LGM, ~21–19 ka), North Atlantic climate has experienced abrupt climate changes, notably the cooling associated with Heinrich event 1 (H1, ~17 ka) and the subsequent warming at the onset of the Bølling–Allerød (BA, ~14.5 ka) (e.g., Heinrich 1988; Dansgaard et al. 1993). One widely accepted hypothesis (e.g., McManus et al. 2004; Boyle and Keigwin 1987) is that these abrupt climate events are causally linked with the stability of the Atlantic meridional overturning circulation

Published online: 25 May 2014

(AMOC). Particularly, the freshwater discharge from ice-sheet melting into the North Atlantic can trigger transitions on a bi-stable AMOC between the active and collapsed states (e.g., Stommel 1961; Bryan 1986; Rahmstorf et al. 2005; Manabe and Stouffer 1988), which leads to a sudden climate cooling or warming during the glacial-interglacial cycle. Nevertheless, this hypothesis has not yet been verified in any deglacial simulations by the state-of-art coupled general circulation models (CGCMs). For instance, a recent CGCM simulation so called TraCE-21 (Transient Climate Evolution of the Last 21,000 Years, Liu et al. 2009; Shakun et al. 2012) successfully reproduces several major climate events (such as H1, the BA) of the last deglaciation, but meanwhile, presents a mono-stable AMOC behavior in response to deglacial meltwater forcing, such that an abrupt climate change can only be generated in response to an abrupt change in the meltwater forcing. The model simulation therefore appears inconsistent with the proxy-based hypothesis.

Customarily, a most desirable way to address above issue is to diagnose the AMOC stability by a suite of stability indicators. The early indicator was proposed by Rahmstorf (1996) as F_{ov}, the overturning part of freshwater transports across the southern boundary of the Atlantic. Later on, F_{ov} was refined to ΔM_{ov}, a net freshwater transport by the AMOC within the Atlantic between the southern and northern boundaries (Dijkstra 2007; Huisman et al. 2010; Liu and Liu 2013, 2014). Both indicators, however, are based on an active AMOC in an idealized equilibrium state but not applicable to a slow evolving AMOC during the last deglaciation. Upon that a generalized stability indicator L is created (Liu et al. 2013, note here an equivalent version of L is also posted in Sijp et al. 2012 and Sijp 2012) for the latter situation. In this study, we will first utilize the indicator L to explicitly estimate the stability of the deglacial AMOC.

Also, we notice that the stability indicators can facilitate the interpretation of the AMOC mono-stable behaviors in CGCMs as well as a potential improvement of deglacial simulations. Based on the stability indicator, several analyses reveal a negative salinity bias commonly existing in most GCCMs under the modern climate in the upper levels of the South Atlantic, which causes a reduced export of freshwater by the AMOC, distorts F_{ov} or ΔM_{ov} towards positive and finally leads to a mono-stable present day AMOC (Weber et al. 2007; Cimatoribus et al. 2012; Jackson 2013; Liu et al. 2014). Provided this salinity bias is an intrinsic deficiency in CGCMs, a similar case is then expected in the LGM climate, i.e., a seeming mono-stable LGM AMOC (e.g., Weber and Drijfhout 2007) might be a biased model result. Moreover, even the initial AMOC is found to be mono- or bi-stable at the LGM, it is plausible to speculate that the AMOC stability can be modulated subsequently by various climate forcings and climate feedbacks during the course of deglacial evolution. In such a case, a careful analysis of L is highly needed to clarify the effects of the model bias, the deglacial climate forcing and the induced climate feedbacks on the stability of the deglacial AMOC.

The rest of the paper is structured as follows. Section 2 provides the information regarding the model and experimental design. In Sect. 3, we estimate and analyze the AMOC stability during the last deglaciation by means of L, especially focusing on the climate feedbacks in modulating the freshwater budget over the Atlantic. In Sect. 4, we expound the implications by L to deglacial simulations by the state-of-art CGCMs. Concluding remarks and further discussions are given in Sect. 5.

2 Model and experiments

The CGCM employed in this study is the Community Climate System Model version 3 (CCSM3) from the National Center for Atmospheric Research (NCAR; Collins et al. 2006), at T31_gx3v5 resolution (Yeager et al. 2006) and with a dynamic global vegetation module. The atmospheric model is the Community Atmospheric Model 3 (CAM3) with 26 hybrid coordinate levels in the vertical and ~3.75-degree resolution in the horizontal. The land model shares the same resolution with the atmosphere. The ocean model is the NCAR implementation of the Parallel Ocean Program (POP) in vertical z-coordinate with 25 levels. The longitudinal resolution is 3.6-degree and the latitudinal resolution is variable, with finer resolution near the equator (~0.9 degrees). The sea ice model is the NCAR Community Sea Ice Model (CSIM), a dynamic thermodynamic model that includes a subgrid-scale ice thickness distribution. The resolution of CSIM is identical to that of POP. Because of rotating the North Pole to Greenland, resolutions of the ocean and ice models become

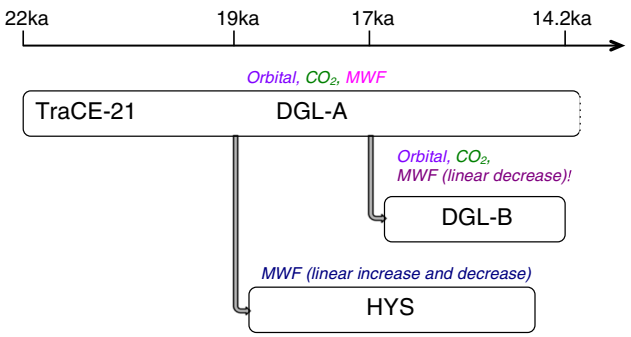

Fig. 1 *Chart* which illustrates the succession of experiments by using NCAR CCSM3 and highlights the setting of several climate forcings. For the description of the experiments and forcings, see the main text

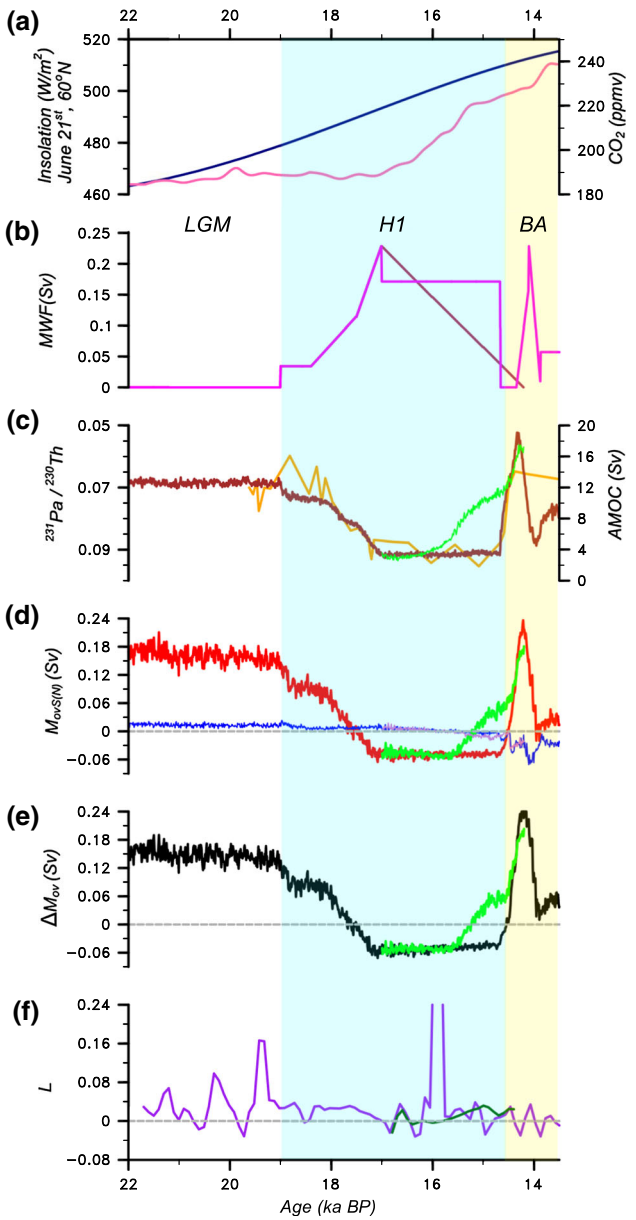

Fig. 2 **a** June insolation at 60°N (*navy*) and atmospheric CO_2 concentration (*pink*). **b** Meltwater fluxes (MWF) imposed in the model. Before the BA (14.35 ka), all the freshwater fluxes are imposed in the Northern Hemisphere (NH), mostly into the North Atlantic (50–70°N) and partly into the Gulf of Mexico. Between 14.35 and 13.87 ka, additional freshwater fluxes are imposed into the Weddell Sea and the Ross Sea. Also, from H1 (17 ka) to the BA, two deglacial scenarios are adopted, respectively as DGL-A (*magenta*) and DGL-B (*dark orchid*), see more details in the main text. **c** Pa/Th ratio (*orange*) at Bermuda (GGC5 core) as a proxy for the AMOC strength, and the model AMOC strength ψ (the maximum transport below 500 m in the North Atlantic) in DGL-A (*brown*) and DGL-B (*light green*). Here, ψ is shown as a decadal mean. **d** The AMOC induced freshwater transports at the southern boundary M_{ovS} (DGL-A, *red*; DGL-B, *light green*) and at the northern boundary M_{ovN} (DGL-A, *blue*; DGL-B, *light orchid*). M_{ovS} and M_{ovN} are calculated by Eqs. (1) and (2) from monthly model outputs and shown in figure as a decadal mean. **e** The net freshwater transport induced by the AMOC across the Atlantic basin, $\Delta M_{ov} = M_{ovS} - M_{ovN}$ (DGL-A, *black*; DGL-B, *light green*). **f** The AMOC stability indicator $L = \partial\overline{\Delta M_{ov}}/\partial\overline{\psi}$ (DGL-A, *purple*; DGL-B, *dark green*) where $\overline{\psi}$ and $\overline{M_{ov}}$ are the AMOC strength and the net AMOC-induced freshwater transport from an (quasi-) equilibrium state. In the calculation, $\overline{\psi}$ and $\overline{\Delta M_{ov}}$ are taken as the 300-year running mean values to eliminate the AMOC inter-decadal variability. The sign of L is not sensitive to the averaging span of ψ and ΔM_{ov} as long as it is beyond the inter-decadal time scale (Liu et al. 2013)

significantly finer towards Greenland. So the narrow straits or passages around the Arctic and the North Atlantic, such as the Fram Strait and the Canadian Arctic Archipelago (CAA), can be well resolved. Additionally, a dynamic global vegetation model is included to reduce the model drift in the deep ocean.

The base-line simulation of this study is TraCE-21 (Fig. 1), whose LGM state is well consistent with a previous LGM study using the standard version of CCSM3 (Otto-Bliesner et al. 2006). TraCE-21 starts at 22 ka, with a transient orbital parameter (navy line in Fig. 2a) and transient concentrations of greenhouse gases (GHGs, such as CO_2, CH_4 and N_2O; Joos and Spahni 2008; see pink line in Fig. 2a for CO_2). According to the ICE-5G reconstruction (Peltier 2004), the height and extent of the continental ice sheets in the simulation are modified, once per 1,000 years prior to 13.1 ka and approximately once per 500 years afterwards. The coastlines at the LGM are also taken from the ICE-5G reconstruction, without any modification before 13.1 ka. In this study, we confine our focus on the deglacial period prior to 13.1 ka (from the LGM to the BA), since the AMOC and its stability could be significantly modulated by the topography change after 13.1 ka, such as the Bering Strait (BS) opening around 12.9 ka. The BS effect (Hu et al. 2007, 2008, 2010, 2012; Liu et al. 2013) and other topography effects on the deglacial AMOC stability are beyond the scope of this paper and we will leave them for future studies. For the effects of orbital forcing, GHGs and continental ice sheets, they turn out to be insignificant. We will discuss this point in Sect. 5.

The meltwater forcing scheme is a most challenging issue for TraCE-21. In the simulation, the locations and the rate of meltwater flux (MWF) are selected to be consistent with the proxy records of sea-level rise (Peltier 2004; Clark and Mix 2002), ice sheet retreat and meltwater discharge (e.g., Clark et al. 2001, 2002; Carlson 2009), the simulated AMOC strength (McManus et al. 2004; Stanford et al. 2006; Praetorius et al. 2008) and the Greenland surface air temperature (SAT; Alley 2000; Cuffey and Clow 1997). From 19 to 17 ka, a MWF input is derived from the Northern Hemisphere (NH) ice sheets to the North Atlantic between 50°N and 70°N and Gulf of Mexico at a rate consistent (within uncertainties) with the record of sea-

level rise (Peltier 2004; Lynch-Stieglitz et al. 2007). As shown in Fig. 2b, the first pulse of MWF is imposed from 19 to 18.4 ka, at the rate of 0.0345 Sv over the North Atlantic. Then in the following 900 years, the MWF linearly increased from 0 to 0.0575 Sv in the Gulf of Mexico and from 0.0343 to 0.0575 Sv in the North Atlantic. Between 17.5 and 17.0 ka, the MWF stays at 0.0575 Sv in the Gulf of Mexico but linearly increases from 0.0575 to 0.1725 Sv in the North Atlantic, so that the MWF reaches a peak flux of 0.23 Sv at 17 ka. Afterwards, the MWF is designed to decrease in two scenarios: a linear decrease to zero at 14.2 ka (DGL-B) and a constant flux (of 0.1725 Sv) until a sudden termination at 14.67 ka (DGL-A). The reason is that, both DGL-A and DGL-B can be considered to represent two extreme situations of possible MWFs largely consistent with the meltwater reconstruction.

In addition, a sensitivity experiment (HYS) is performed (Liu et al. 2013) to test the dependence of the AMOC stability on various climate forcings. HYS is initialized from the state of 19.0 ka in TraCE-21 and maintains a constant orbital forcing and GHG concentrations at 19.0 ka throughout the simulation. The MWF is distributed uniformly in the North Atlantic domain within 50–70°N, and the magnitude increases linearly from zero and increases by 0.086 Sv per thousand year in the first 2,000 years and then reduces linearly by 0.086 Sv per thousand year in the latter 2,000 years. Overall, the hosing (de-hosing) processes of HYS are analogous to those in DGL-B. Although with a weaker hosing rate, the AMOC in HYS virtually collapses at the maximum hosing. Moreover, it exhibits a linear response to the MWF perturbations. The AMOC is then suggested to reside in a mono-stable regime. Since HYS follows a general approach of the AMOC hysteresis test (e.g., Rahmstorf 1996; Rahmstorf et al. 2005) and meanwhile, acts to mimic the deglacial process in a most simple way, it can be used as a benchmark for the following analyses of the AMOC stability in TraCE-21. Here, by following the chronology in TraCE-21, HYS lasts from 19 to 15 ka, with the MWF reaching its peak of 0.172 Sv at 17 ka.

3 Results

3.1 The stability of the deglacial AMOC

First, we examine the stability of the deglacial AMOC in TraCE-21. Figure 2c illustrates the AMOC response to the input of MWF during the deglacial evolution. Starting from 19 ka, the increase of MWF causes a gradual decrease in the AMOC, whilst from 17 ka to the BA, the decrease in MWF induces an increasing the AMOC, either in DGL-A or DGL-B. In the former experiment, the AMOC resumes abruptly at the BA (brown line in Fig. 2c) with an abrupt termination of MWF (magenta line in Fig. 2b), as consistent with a reconstruction of the proxy record at Bermuda (GGC5 core; McManus et al. 2004; see orange line in Fig. 2c). In the latter, the AMOC recovers gradually towards the BA (green line in Fig. 2c) following the gradual decrease of MWF (dark orchid line in Fig. 2b). Therefore, regardless of the recovery speeds in different scenarios, the AMOC appears a quasi-linear response to MWF between 19 and 14.2 ka, suggesting a mono-stable circulation during the last deglaciation.

The mono-stability of the AMOC can be further interpreted by a basin-scale salinity advection feedback via a generalized stability indicator of L (Liu et al. 2013). For a slowly evolving deglacial AMOC, the circulation can induce an overturning component of freshwater transport

$$M_{ov} = \int_{-H}^{0} m_{ov}(z)dz \tag{1}$$

across an arbitrary section in the Atlantic. Here H is the depth of the sea bottom along the section and

$$m_{ov}(z) = (-1/S_0)v(z)\{s(z) - S_0\} \tag{2}$$

where v is the velocity normal to the section and s is the salinity at the section. The angle and curly brackets indicate the along-section mean and integration, respectively. S_0 is a reference salinity and taken as the Atlantic basin mean salinity. Over the Atlantic, the net freshwater transport induced by the AMOC is $\Delta M_{ov} = M_{ovS} - M_{ovN}$ where M_{ovS} and M_{ovN} are the freshwater transports at the southern ($\sim$34°S) and northern ($\sim$80°N) boundaries. Note here, because of a closed BS prior to 13.1 ka, there is no meridional barotropic transport in the Atlantic. As such, M_{ovS} is equivalent to F_{ov} (Rahmstorf 1996) or M_{34S} (Drijfhout et al. 2011). For M_{ovN}, it equals to the sum of the overturning liquid freshwater transports across the CAA (M_{ovCAA}), the Fram Strait (M_{ovFRA}) and the western shelf of the Barents Sea (M_{ovBAR}). Again, due to the closure of the CAA and Barents Sea prior to 13.1 ka, $M_{ovCAA} = M_{ovBAR} = 0$, so that $M_{ovN} = M_{ovFRA}$.

Based on ΔM_{ov}, we then define a generalized indicator of the AMOC stability, $L = \partial\overline{\Delta M_{ov}}/\partial\overline{\psi}$ where $\overline{\psi}$ and $\overline{\Delta M_{ov}}$ are the AMOC strength and the net AMOC-induced freshwater transport from an (quasi-)equilibrium state. This generalized indicator represents a basin-scale salinity advection feedback related to the AMOC. A positive L indicates a negative feedback and a mono-stable AMOC, because an initial weakening (strengthening) of the AMOC will induce an anomalous freshwater convergence (divergence) and salinify (freshen) the Atlantic basin, which promotes (inhabits) the deep convection in the North Atlantic and leads to a strengthening (weakening) of the

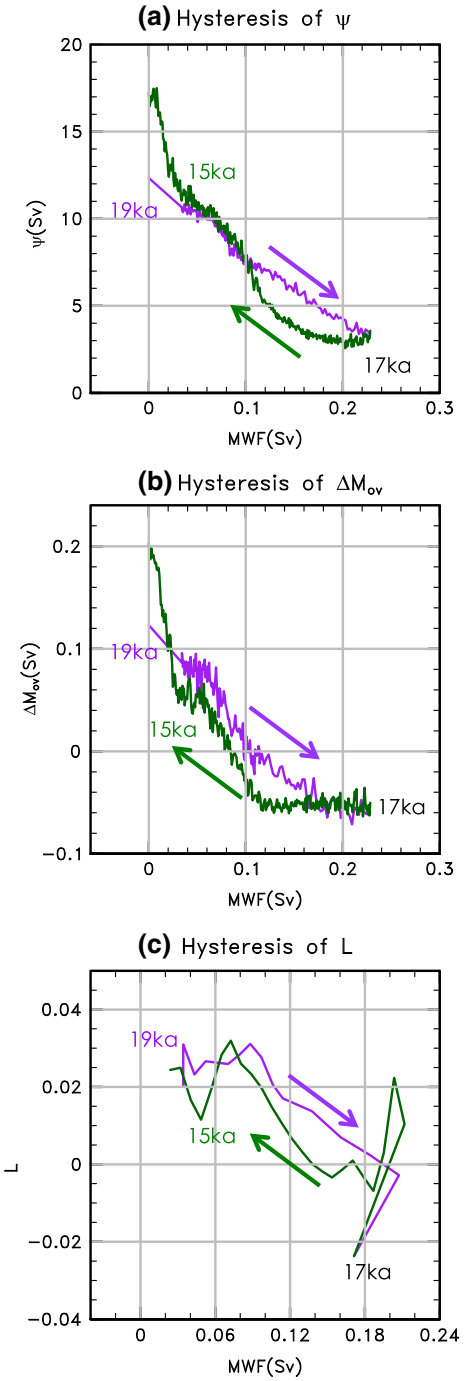

Fig. 3 "Hysteresis diagram" showing **a** the AMOC strength ψ, **b** the net freshwater transport induced by the AMOC and **c** the AMOC stability indicator L as a function of the prescribed meltwater flux in DGL-B. In the calculation of L, $\overline{\psi}$ and $\overline{\Delta M_{ov}}$ are taken as the 300-year running mean values to eliminate the AMOC inter-decadal variability. Arrows and three time points (19, 17 and 15 ka) are labeled in each *plot* as auxiliary indications of the progression of the relationships between transport/circulation and freshwater flux. Particularly, the *purple curve* (*arrow*) denotes the evolution from 19 to 17 ka whilst the *dark green curve* (*arrow*) denotes the evolution from 17 to 15 ka and then on

AMOC. On the other hand, a negative L suggests a positive feedback and a bi-stable AMOC by a similar argument. As illustrated in Figs. 2f and 3, $\overline{\psi}$ and $\overline{\Delta M_{ov}}$ appear to exist a general linear relationship during the last deglaciation so that L stays mostly positive in either DGL-A or in DGL-B, suggesting a mono-stable AMOC during the deglaciation in CCSM3.

The mono-stable deglacial AMOC can be further seen in the "hysteresis diagram" from the scenario of DGL-B, with $\overline{\psi}$, $\overline{\Delta M_{ov}}$ and L being plotted against the MWF (Fig. 3). At 19 ka, the diagram shows a vigorous LGM AMOC inducing a freshwater convergence ($\Delta M_{ov} > 0$) across the Atlantic basin. When the MWF increases in H1 (colored purple), the AMOC diminishes almost linearly and the freshwater convergence reduces to zero and then switches to a freshwater divergence ($\Delta M_{ov} < 0$). Around the MWF maximum at 17 ka, the AMOC stays a transient off-mode, with a freshwater divergence in a short period. Later on, with a decrease in the MWF (colored dark green), the AMOC and ΔM_{ov} largely follows a trajectory of gradual recovery, which results in an indistinctive hysteresis loop either in $\psi$and ΔM_{ov}, as the characteristic of a mono-stable AMOC.

3.2 The deglacial M_{ovS}

Based on above analyses, the key for diagnosing the deglacial AMOC stability indicator is the evolution pattern of ΔM_{ov} and its relationship to the AMOC transport (ψ) during the deglacial processes. Figure 2 shows that the evolution pattern of ΔM_{ov} (in panel e, black line for DGL-A and green line for DGL-B) before the BA is dominantly determined by that of M_{ovS} (in panel d, red line for DGL-A and green line for DGL-B), which switches from a freshwater import of $\sim$0.15 Sv at 19 ka to a freshwater export of $\sim$0.06 Sv at 17 ka. Meanwhile, M_{ovN} (in panel d, blue line for DGL-A and light orchid line for DGL-B) has a small amplitude with little variations due to a BS closure and a partly undermined BS effect in the cold LGM climate (Liu et al. 2013). Therefore, in the following, we take $\Delta M_{ov} \approx M_{ovS}$ and focus on M_{ovS}, more specifically, its vertical profile, m_{ovS} (the value of m_{ov} at 34°S), to further investigate the mechanism on the mono-stability of the deglacial AMOC.

Figure 4a shows m_{ovS} at 19 ka. The surface water, the thermocline water and North Atlantic Deep Water (NADW) at 34°S are fresher than S_0, whereas the former two water masses are fresher than NADW (Fig. 4a), so the AMOC induces a freshwater import of 0.243 Sv via its upper limb but a smaller freshwater export of 0.043 Sv via its lower limb. That is to say, the AMOC induces a net

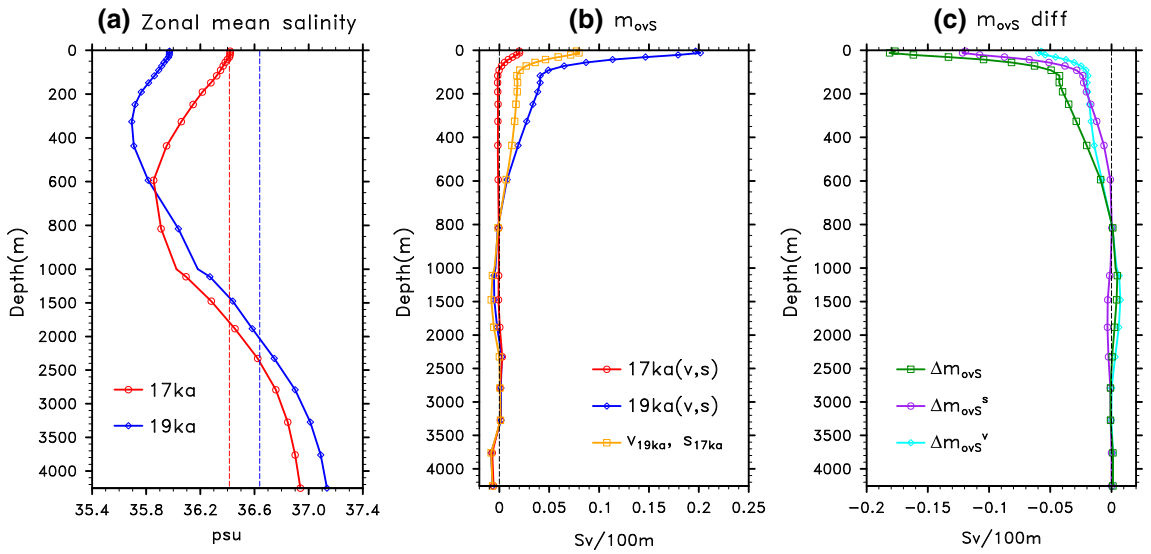

Fig. 4 Vertical profiles of **a** zonal mean salinity along 34°S at 17 ka (*red*) and 19 ka (*blue*); **b** the overturning component m_{ovS} at 17 ka (*red*) and 19 ka (*blue*) as well as the one (*orange*) calculated from the velocity at 19 ka and the salinity at 17 ka; **c** the m_{ovS} difference between 19 and 17 ka (17 ka minus 19 ka), Δm_{ovS}(*dark green*) that divided as Δm^s_{ovS} (*purple*), a contribution due to salinity change and Δm^v_{ovS} (*cyan*), a contribution due to velocity change from 19 to 17 ka. See main text for more details

freshwater import of 0.2 Sv at 34°S. On the other hand, Antarctica Bottom Water (AABW) is saltier than S_0 and the salinity gradient increases downward, leading to a freshwater export of 0.046 Sv by the AABW cell. The total vertical integration of m_{ovS} over the entire depth yields a freshwater import of $M_{ovS} = 0.154\ Sv$.

From 19 ka to 17 ka, M_{ovS} switches from a freshwater import to a freshwater export, as a result of a large decrease in the freshwater import of the surface and thermocline waters, a relatively smaller decrease in the freshwater export of NADW and a negligible decrease in the freshwater export of AABW (Fig. 4c). This deglacial change in M_{ovS} (colored dark green), however, can be caused by two factors, the change in velocity or in salinity. Here, to quantify the individual contribution from each factor, we calculate the difference of m_{ovS} between 19 ka and 17 ka

$$\Delta m_{ovS} = \Delta m_{ovS(17ka)} - \Delta m_{ovS(19ka)} \tag{3}$$

and divides it into two parts

$$\Delta m_{ovS} = \Delta m^s_{ovS} + m^v_{ovS} \tag{4}$$

where Δm^s_{ovS}, Δm^v_{ovS} are the contributions from the salinity and velocity fields, respectively. In particular, Δm^s_{ovS} is calculated by the formula

$$\begin{aligned}\Delta m^s_{ovS} = {} & (-1/S_0)v_{19ka}\{s_{17ka} - S_0\} \\ & - (-1/S_0)v_{19ka}\{s_{19ka} - S_0\}\end{aligned} \tag{5}$$

where v_{19ka} and S_0 are the velocity and the reference salinity at 19 ka, s_{19ka} and s_{17ka} are salinities respectively at 19 and at 17 ka. Δm^v_{ovS} is calculated as the difference between Δm_{ovS} and Δm^s_{ovS}.

Figure 4c displays the vertical profiles of Δm^s_{ovS} (colored purple) and Δm^v_{ovS} (colored cyan) between 19 and 17 ka (17 ka minus 19 ka). In the upper branch of the AMOC (above 800 m), the northward flow decreases due to a collapse of the AMOC (Figs. 2c, 5). In the mean time, the surface and thermocline waters are salinified (Fig. 4a), suggesting that both Δm^v_{ovS} and Δm^s_{ovS} contribute to a decrease of the freshwater import in this layer. Quantitatively, the vertical integrations of Δm_{ovS}, Δm^s_{ovS} and Δm^v_{ovS} equal to −0.242, −0.118 and −0.124 Sv, respectively, such that either of m^s_{ovS} and Δm^v_{ovS} contributes about half of the reduction in the freshwater import. In the lower branch of the AMOC (800–2,000 m), the southward flow weakens and carries a smaller amount of freshwater out of the Atlantic basin ($\Delta m^v_{ovS} > 0$). Meanwhile, NADW is freshened by the input of MWF, so the AMOC exports a diluted water mass out of the Atlantic basin ($\Delta m^s_{ovS} < 0$). The vertical integrations of Δm_{ovS}, Δm^v_{ovS} and Δm^s_{ovS} in this layer amount only to −0.037, 0.069 and −0.032 Sv, respectively. Thus Δm^v_{ovS} is stronger than, and is partly cancelled by Δm^S_{ovS}. The analyses above suggest that the salinity increase in the surface and thermocline waters (along 34°S) is critical to the sign switch of M_{ovS} during the last deglaciation.

3.3 The salinified upper ocean at 34°S

To understand why the upper ocean at 34°S is salinified during the last deglaciation, we start from a view of deglacial changes in the sea surface salinity (SSS). From 19 to 17 ka, the surface water becomes saltier in the South

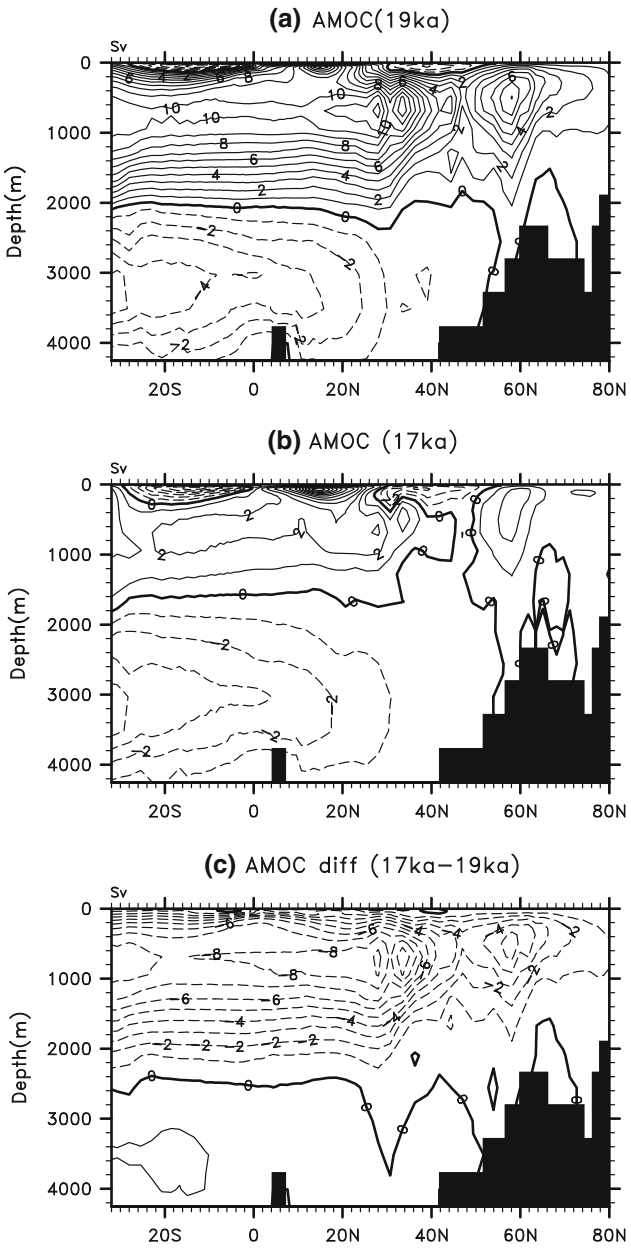

Fig. 5 Atlantic overturning streamfunction (*contoured* in Sv) in **a** 19 ka and **b** 17 ka. Plot **c** displays the difference between **a** and **b**. Streamfunction is calculated as a 100-year mean

Atlantic, ranging from 20°S to the southern border of 34°S, with a poleward extent to 44°S (Fig. 6a). Based on previous studies (Provost et al. 1999; Donners et al. 2005), the surface water ventilates in the region of 40–44°S and subducts as the South Atlantic Subtropical Mode Water (SASTMW), which seems also to be case here, in TraCE-21. As shown in Fig. 6a, the saltier water around 40°S subducts along the isopycnals, shaping a salt tongue in subsurface and leading to a salinity increase in the thermocline water at 34°S.

Thus, we have found that changes in the SSS are mostly generated by changes in the surface freshwater (*FW*) forcing over the South Atlantic. From 19 to 17 ka, the South Atlantic generally experiences a freshwater gain between equator and 20°S but a freshwater loss between 20°S and 44°S (Fig. 7b), which respectively induces a decrease and an increase of salinity in the surface water. To probe into the mechanism of the *FW* change, we decompose *FW* into four components: precipitation (*P*), evaporation ($-E$), runoff (R) and the sea-ice melting and brine rejection ($M - B_r$). Hence from 19 to 17 ka, the *FW* change can be written as

$$\Delta FW = \Delta P + \Delta(-E) + \Delta R + \Delta(M - B_r) \quad (6)$$

Figure 7b clearly shows that the freshwater gain between equator and 20°S mainly comes from an increased precipitation in the tropical South Atlantic, because of a well-known southward Intertropical Convergence Zone (ITCZ) shift in response to the AMOC shutdown (e.g., Zhang and Delworth 2005; Stouffer et al. 2006; Kageyama et al. 2013) by mechanism of the wind-evaporation-SST (WES) feedback (e.g., Xie and Philander 1994; Xie 1996; Chang et al. 1997). On the other hand, the freshwater loss in the mid-latitude South Atlantic between 20°S and 44°S is primarily caused by an increased evaporation in this region. In contrast to the mid-latitude South Atlantic region, evaporation does not change significantly during the deglaciation in the tropical South Atlantic between the equator and 20°S. A further analysis shows that evaporation in the tropical Atlantic is not changed because the enhanced partition due to the warmer sea surface temperature (SST) is largely cancelled by the reduced partition associated with the weakened trade winds. In contrast, in the mid-latitude South Atlantic, the deglacial SST warming is accompanied by little changes of the wind intensity. This leads to an enhanced evaporation and, in turn, salinification in the upper ocean at 34°S. Figure 8c displays the deglacial change of SST over the Atlantic. Due to the freshwater discharge by ice sheet melting into the North Atlantic, a shutdown of the AMOC disrupts the meridional heat transport from low latitudes to the North Atlantic, leading to a bipolar seesaw response (e.g., Blunier and Brook 2001; Barker et al. 2009): a sharp cooling in the North Atlantic and a warming in the South Atlantic. Analogous to the Atlantic meridional mode (AMM; see references, e.g., Chiang and Vimont 2004; Xie and Carton 2004), this dipole-like SST response across the equator (Fig. 8e) induces an anomalous cross-gradient flow from the NH to the Southern Hemisphere (SH), intensifies the trade winds in the NH but weakens the trade winds in the SH (similar patterns can be also seen from references, e.g., Dong and Sutton 2002; Krebs and Timmermann 2007; Wu et al. 2008). Then between the equator and 20°S, the SST

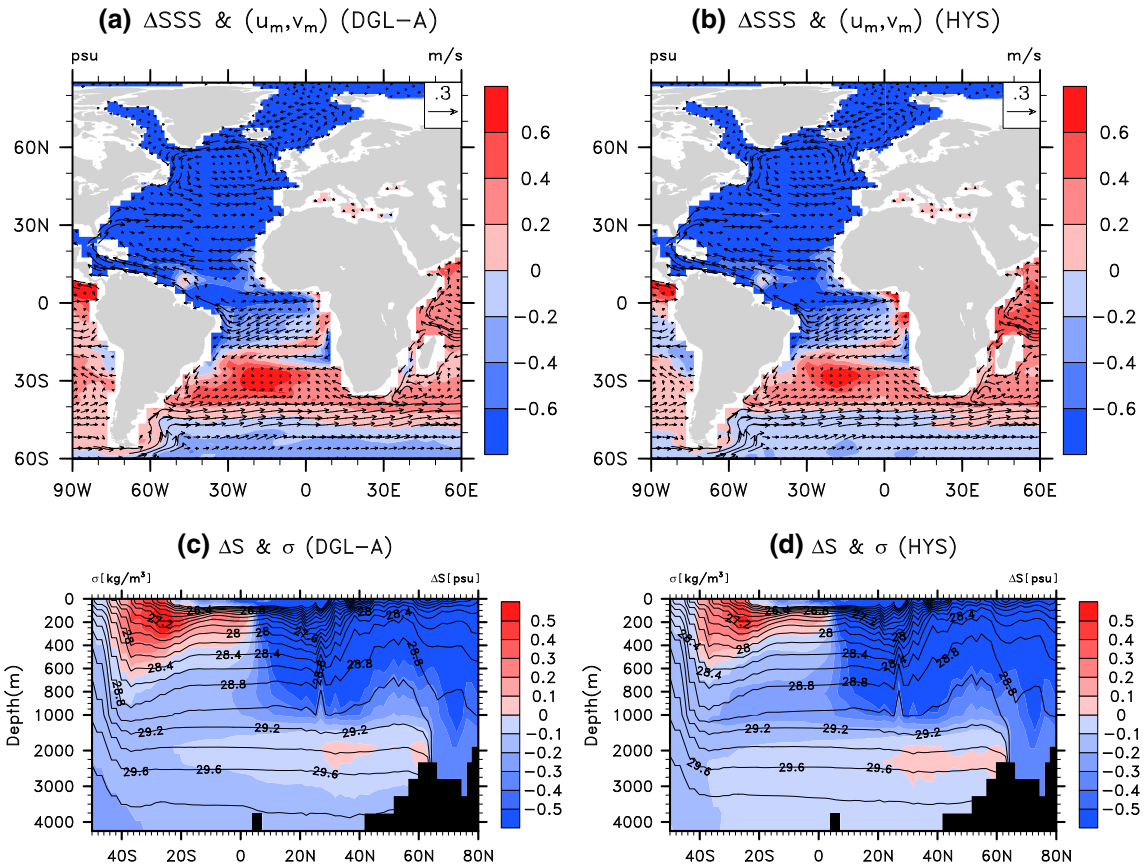

Fig. 6 (*top panel*) Maps of changes (from 19 to 17 ka) in the sea surface salinity (SSS, *contour shading* in psu) and surface oceanic currents (*vectors* in unit of m/s) over the Atlantic from **a** DGL-A and **b** HYS simulations. (*bottom panel*) Depth-latitude diagrams of changes (from 19 to 17 ka) in the zonal average salinity (*shading* in psu) and potential density σ (*contour* in kg/m^3) in the Atlantic from **c** DGL-A and **d** HYS simulations. Salinity, oceanic current and potential density shown in the figure are calculated as a 100-year mean

increases but the wind strength decreases, i.e., the SST and the wind impose opposite effects on evaporation, so that evaporation over this region does not exhibit significant variations from 19 ka to 17 ka (Fig. 7c).

It is worth noting that the deglacial freshwater change by runoff may also play a role in salinifying the upper ocean at 34°S. From 19 to 17 ka, owing to a reduced riverine discharge (Fig. 7d), two tongues of positive SSS anomalies appear at the eastern equatorial Atlantic near the exits of the Sanaga and Nyong Rivers as well as the Congo River. These anomalously saltier waters are then carried by a southwestward branch of the South Equator Current (SEC) to join the recirculation gyre in the South Atlantic (Fig. 6a), contributing to the salinification within 20-44°S. This reduced river discharge appears to be consistent with proxy records. A proxy record of Core GeoB4905-4 (2.5°N, 9.4°E; 1,328 m) off Cameroon (Adegbie et al. 2003) shows a deglacial SSS increase near the Sanaga and Nyong Rivers' mouth from 19 to 17 ka (Fig. 9). According to Weldeab et al. (2005), these local SSS variations are likely related to the deglacial changes in the African monsoon system (AMS), more specifically, the change in regional patterns of precipitation over the equatorial western Africa.

4 Implications

As learned from Fig. 4, M_{ovS} is affected partly by NADW through its lighter return flow and partly by AABW in its deep return flow. Therefore, M_{ovS} can be decomposed into two components: one associated with deep-water formation in the North Atlantic, M_{ovS}^{NA}, and the other associated with deep-water formation in the Southern Ocean, M_{ovS}^{SO} (Drijfhout et al. 2011). The boundary between the two is where

Fig. 7 Maps of surface freshwater changes over the Atlantic from 19 to 17 ka. (*top two panels*) Maps of changes in **a** net freshwater flux, **b** precipitation, **c** evaporation, **d** runoff and **e** sea-ice melting and brine rejection in DGL-A. (*bottom two panels*) Maps of changes in **f** net freshwater flux, **g** precipitation, **h** evaporation, **i** runoff and **j** sea-ice melting and brine rejection in HYS. Fluxes in figure are shown in mm/day and calculated as a 100-year mean

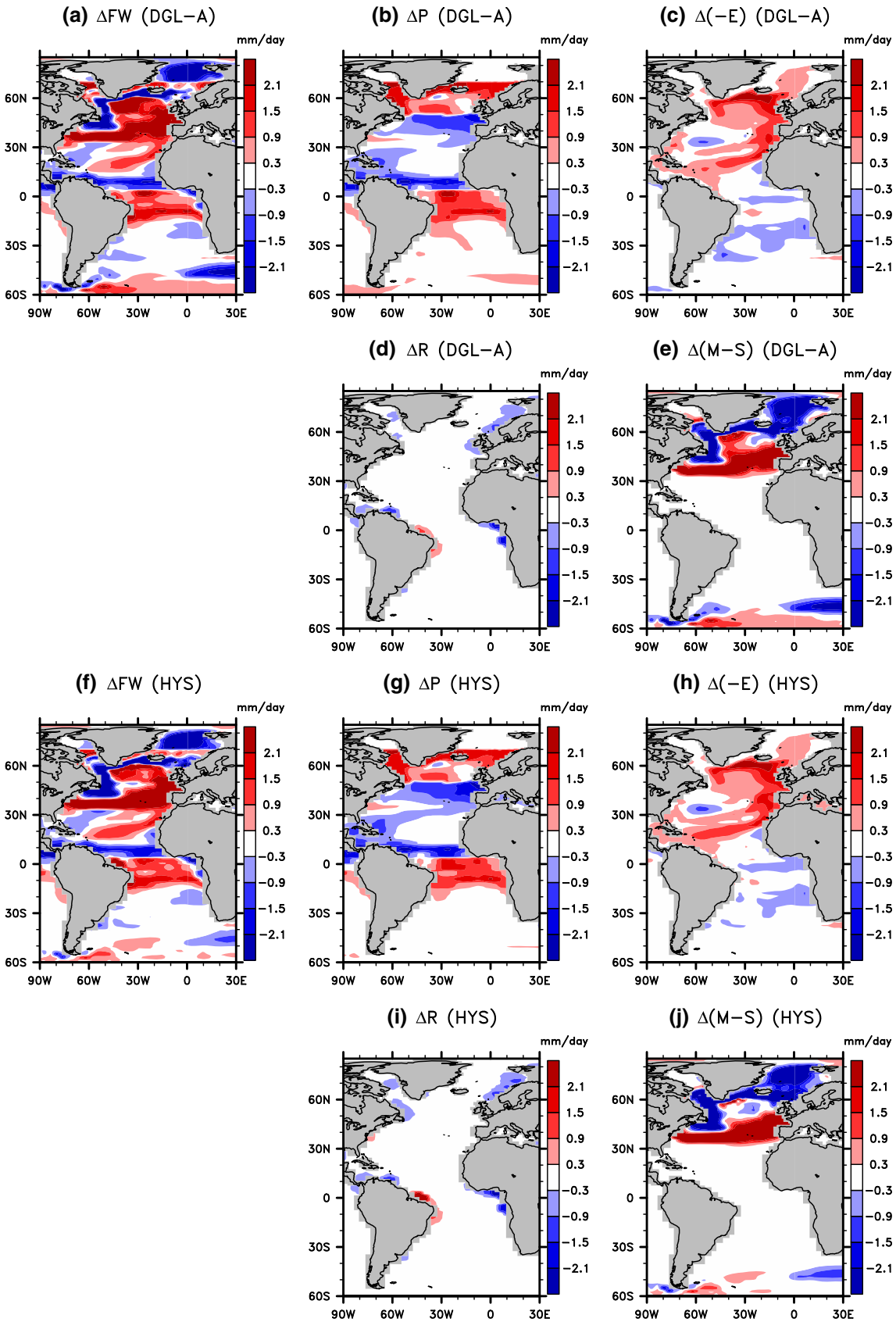
(a) ΔFW (DGL−A)
(b) ΔP (DGL−A)
(c) Δ(−E) (DGL−A)
(d) ΔR (DGL−A)
(e) Δ(M−S) (DGL−A)
(f) ΔFW (HYS)
(g) ΔP (HYS)
(h) Δ(−E) (HYS)
(i) ΔR (HYS)
(j) Δ(M−S) (HYS)
mm/day
2.1
1.5
0.9
0.3
−0.3
−0.9
−1.5
−2.1
60N
30N
0
30S
60S
90W
60W
30W
0
30E

the AMOC streamfunction becomes zero. Herein the stability indicator L can be written as

$$L = \partial\overline{\Delta M_{ov}}/\partial\overline{\psi} = \partial\overline{M_{ovS}^{NA}}/\partial\overline{\psi} + \partial\overline{M_{ovS}^{SO}}/\partial\overline{\psi} + \left(-\partial\overline{M_{ovN}}/\partial\overline{\psi}\right) \quad (7)$$

From 19 to 17 ka, M_{ovS}^{NA}, M_{ovS}^{SO} and M_{ovN} have changed by −0.242, 0.006 and −0.003 Sv, respectively. The last two terms in Eq. (7), $\partial\overline{M_{ovS}^{SO}}/\partial\overline{\psi}$ and $\left(-\partial\overline{M_{ovN}}/\partial\overline{\psi}\right)$, are at least one order smaller than $\partial\overline{M_{ovS}^{NA}}/\partial\overline{\psi}$. Meanwhile, M_{ovS}^{NA} can be approximately estimated as

$$M_{ovS}^{NA} \approx (-1/S_0)\psi \cdot \Delta s \quad (8)$$

where Δs denotes the salinity contrast between the upper and lower limbs of the AMOC, i.e., the salinity of the surface and thermocline waters minus the salinity of NADW. Inserting Eq. (8) into Eq. (7) and denoting $\partial\overline{M_{ovS}^{SO}}/\partial\overline{\psi}$ and $\left(-\partial\overline{M_{ovN}}/\partial\overline{\psi}\right)$ as small order terms $O(\mathcal{E}_{SO})$ and $O(\mathcal{E}_N)$, we can obtain

$$L = (-1/S_0)\overline{\Delta s} + (-1/S_0)\overline{\psi} \cdot \left(\partial\overline{\Delta s}/\partial\overline{\psi}\right) + O(\mathcal{E}_{SO}) + O(\mathcal{E}_N) \quad (9)$$

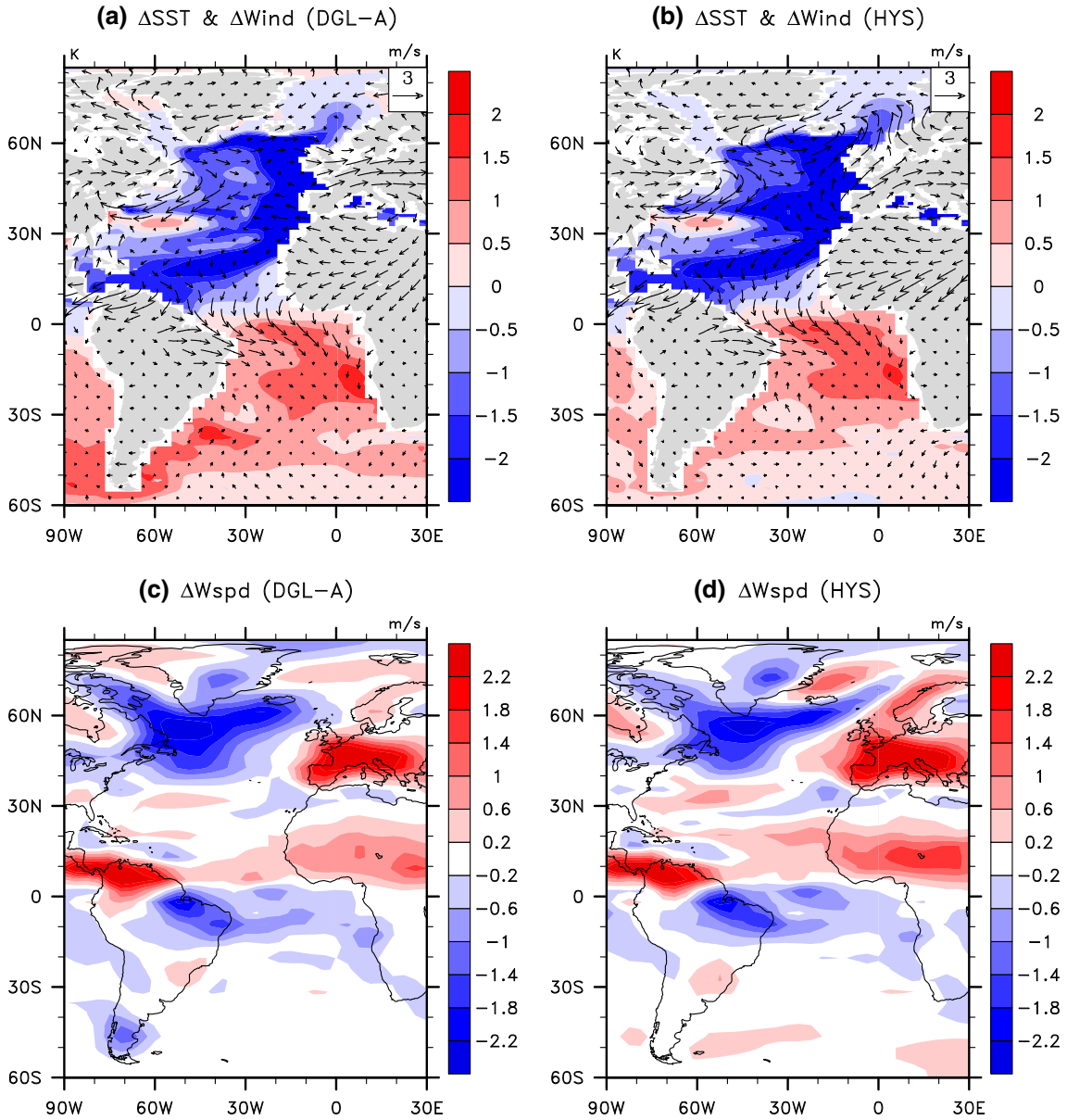

Fig. 8 (*top panel*) Maps of changes (from 19 to 17 ka) in the sea surface temperature (SSS, *contour shading* in Kelvin) and surface winds (*vectors* in unit of m/s) over the Atlantic from **a** DGL-A and **b** HYS simulations. (*bottom panel*) Maps of changes (from 19 to 17 ka) in the surface wind speed (*contour shading* in m/s) over the Atlantic from **c** DGL-A and **d** HYS simulations. Temperature, wind vector and wind speed shown in figure are calculated as a 100-year mean

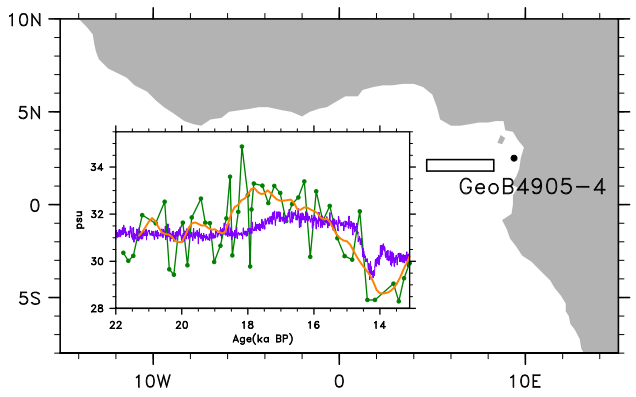

Fig. 9 Map of a proxy record of Core GeoB4905-4 located at (2.5°N, 9.4°E; 1,328 m) off Cameroon (Adegbie et al. 2003). The *inserted* diagram displays the reconstructed SSS from GeoB4905-4 (*green*) and a model SSS from DGL-A (*purple*), i.e., the SSS in a most adjacent grid (*black box*) to Core GeoB4905-4. A smoothed reconstructed SSS (*orange*) is also shown in the diagram, which is calculated in such a way; we first linearly interpolate the reconstructed SSS into a time series with a uniform centenary interval and then apply a 9-point running average on the interpolated series to get the smoothed result

Here, we name $(-1/S_0)\overline{\Delta s}$ and $(-1/S_0)\overline{\psi}\cdot\left(\partial\overline{\Delta s}/\partial\overline{\psi}\right)$ respectively as the stratification term and the feedback term. Then Eq. (9) describes that L is primarily determined by the stratification term (stratification at 34°S) and the feedback term (stratification changes with the AMOC evolution). In the following, we will elaborate implications of each term in Eq. (9) to CGCMs on the deglacial simulation.

4.1 The stratification term $(-1/S_0)\overline{\Delta s}$

First, we would like to clarify that, if $M_{ovS}^{SO} \approx 0$ and therefore it can be ignored (such as the case in modern climate, see Talley 2008), the stratification term will be consistent with the indicator F_{ov} (Rahmstorf 1996); thereby the difference between L and F_{ov} is the feedback term. This additional feedback term enables L to indicate the stability of a slowly evolving AMOC, which is critical to the deglacial simulation by CGCMs.

Then we would like to clarify that the stratification term is usually biased in CGCMs for various reasons, which may lead to a biased AMOC stability in the deglacial simulations by these models. As shown in TraCE-21, the surface and thermocline waters in the South Atlantic are much fresher than NADW during the LGM (Fig. 4a), so that $\Delta s < 0$ and the stratification term is positive, favoring a freshwater import and a mono-stable AMOC. However, from several recent studies (Liu 2012; Jackson 2013; Liu et al. 2014), it is suggested that this negative stratification term could be caused by a bias of the climate models from the real world today and probably at the LGM.

To test the robustness of aforesaid argument, we investigate the LGM simulations from seven CMIP5/PMIP3 (Coupled Model Intercomparison Project Phase 5/Paleoclimate Modelling Intercomparison Project Phase 3) CGCMs (Table 1; Taylor et al. 2012) and compare the model results with observations. Here, in CMIP5/PMIP3 LGM simulations, a 21 ka boundary condition is employed which contains the orbital parameters, GHGs, ice sheet, land-sea mask, etc. (more details can be found at http://pmip3.lsce.ipsl.fr/). For observations, we adopt a reconstructed SSS at the LGM (Schäfer-Neth and Paul 2003) and the proxy data (Adkins et al. 2002) from Ocean Drilling Program (ODP). In the former, the LGM SSS is reconstructed from the updated temperature data and available oxygen isotope measurements, with a salinity anomaly of 1.0 psu added in the Weddell Sea (Fig. 10a). In the latter, the abyssal temperature and salinity at the LGM are reconstructed from ODP data at site 981 in the North Atlantic (Feni Drift 55.48°N, 14.65°W; 2,184 m). Herein it is worth mentioning that, in the surface paleo-observation, the global gridded dataset is available and desirable for the estimation of glacial surface water properties despite some uncertainties in the proxy reconstruction and data gridding. Whilst abyssal paleo-observations are relatively fewer, as such they are so far unavailable along the section of 34°S in the South Atlantic. Thus to estimate the property of glacial NADW at 34°S, we adopt a remote observation at Feni Drift in the North Atlantic, assuming that the properties of NADW (at least the salinity) are conserved over the deep Atlantic (a point to be returned later).

Figure 11 shows the comparison results. In observation, the surface water at 34°S has a salinity of 36.5 psu (denoted by star in panel a and b) and the thermocline water would be even saltier, considering a conventional salinity increase in the thermocline. Whereas NADW at 34°S has a salinity of 36.1 psu (obtained from Feni Drift and denoted by black dot in panel b), so that $\Delta s > 0$ and the stratification term is negative, suggesting a freshwater export and a bi-stable AMOC during the LGM. On the other hand, model results from most CMIP5/PMIP3 CGCMs resemble closely that in CCSM3, in which the surface and thermocline waters are much fresher than NADW (locating at 1,800–3,000 m in most models, as seen from Fig. 12), i.e., $\Delta s < 0$ and the stratification term is positive. Therefore, the stratification term is likely to be biased towards positive in CGCMs. Here, before a further analysis of the salinity bias, it would be good to keep in mind that great uncertainties may exist in the bias estimation of salinity, as considering the uncertainties in the proxy reconstruction and paleo-data gridding.

Table 1 The seven models of CMIP5/PMIP3 and CCSM3 involved in this study and their development groups, model abbreviations, ocean component and time periods of the LGM simulation (for CCSM3, a centenary period of simulation at 21 ka is selected)

Modeling group	Model abbreviation	Ocean component	Period (year)
National Center for Atmospheric Research (NCAR), United States	CCSM4	POP2 60 vertical layers $1.11° \times (0.27° - 0.54°)$	101
Center National de Recherches météorologiques (CNRM)—Centre Européen de Recherche et de Formation Avancée en Calcul Scientifique (CERFACS), France	CNRM-CM5	NEMO v3.2 42 vertical layers, $1° \times (0.33° - 1°)$	200
State Key Laboratory of Numerical Modeling for Atmospheric Sciences and Geophysical Fluid Dynamics (LASG), China	FGOALS-g2	LICOM2 30 vertical layers $\sim 1° \times 1°$	100
National Aeronautics and Spatial Administration (NASA), Goddard Institute for Spatial Studies (GISS), United States	GISS-E2-R	Russell 32 vertical layers $1° \times 1.25°$	100
Japan Agency for Marine-Earth Science and Technology, Atmosphere and Ocean Research Institute, the University of Tokyo and National Institute for Environmental Studies, Japan	MIROC-ESM	COCO v3.4 44 vertical layers $\sim 1.4° \times 1°$	100
Max Planck Institute for Meteorology (MPI-M), Germany	MPI-ESM-P	MPI-OM 40 vertical layers $\sim 1.5° \times 1.5°$	100
Meteorological Research Institute (MRI), Japan	MRI-CGCM3	MRI.COM3 51 vertical layers $1° \times 0.5°$	100
National Center for Atmospheric Research (NCAR), United States	CCSM3	POP 25 vertical layers $3.6° \times (1° - 2°)$	100

This biased stratification term may result from the salinity bias either in the surface and thermocline waters or in NADW. From Fig. 10b–i, a negative SSS bias occurs in the South Atlantic among all the CMIP5/PMIP3 CGCMs. At 34°S, the model salinity has a negative bias of −1.6 psu to −0.6 psu in the surface water (Fig. 11a). Besides, with the subduction of anomalously fresher SASTMW (Fig. 6a), a negative salinity bias is also expected in the thermocline water at 34°S. Meanwhile, as learned from Sect. 3, most of M_{ovS} is induced by the upper limb of the AMOC, hence the negative salinity bias in the surface and thermocline waters, in turn, play a dominant role in biasing the stratification term towards positive in CGCMs.

On the other hand, it seems more complex to estimate the salinity bias of NADW in distorting the stratification term. First, NADW in CGCMs may not share the same properties with the observation. In Fig. 11b, we compare the model salinity with an ODP reconstructed salinity at the same location (Feni Drift 55°N, 15°W; 2,184 m) and find that two CMIP5/PMIP3 models (CCSM4 and MRI-CGCM3) are able to simulate NADW formatted with a similar salinity to the observation. Five CMIP5/PMIP3 models (CNRM-CM5, FGOALS-g2, GISS-E2-R, MIROC-ESM, MPI-ESM-P) generate a negative bias of -0.9psu to -0.2psu while CCSM3 produces a positive bias of 0.2 psu in the salinity of NADW. Additionally, from the model results, the NADW properties could be altered along its path to 34°S, which is most likely relevant to the oceanic diffusivity parameterization in model. In short, it is of great uncertainties to estimate the bias of the stratification term from the salinity bias in NADW.

Fig. 10 **a** The reconstructed SSS at the LGM in the "core" version of the data set (Schäfer-Neth and Paul 2003), in which a salinity anomaly of 1.0 psu added in the Weddell Sea. Against **a**, **b**–**h** illustrates the SSS biases in seven CMIP5/PMIP3 CGCMs, which are calculated by averaging the model SSS over the whole simulation period (Table 1) and then subtracting the reconstructed SSS. **i** The SSS bias in CCSM3. Here, to be consistent with CMIP5/PMIP3 models, the SSS bias in CCSM3 is calculated by averaging the SSS over 100 years at 21 ka and then subtracting the reconstructed SSS. Salinity in figure is shown in the unit of psu ▶

4.2 The feedback term $(-1/S_0)\overline{\psi} \cdot \left(\partial\overline{\Delta s}/\partial\overline{\psi}\right)$

As shown in Sect. 3, the feedback term is related to the climate feedbacks induced by the deglacial change of the AMOC. From 19 to 17 ka, the surface and thermocline water at 34°S is significantly salinified as a result of a bipolar seesaw response in SST with enhanced evaporation in the South Atlantic, whilst the NADW outflow is moderately freshened by the discharge of freshwater from ice sheet melting. Hence the salinity contrast Δs increases with the AMOC shutdown, i.e., the feedback term $(-1/S_0)\overline{\psi} \cdot \left(\partial\overline{\Delta s}/\partial\overline{\psi}\right) > 0$. In brief, the collapse of the

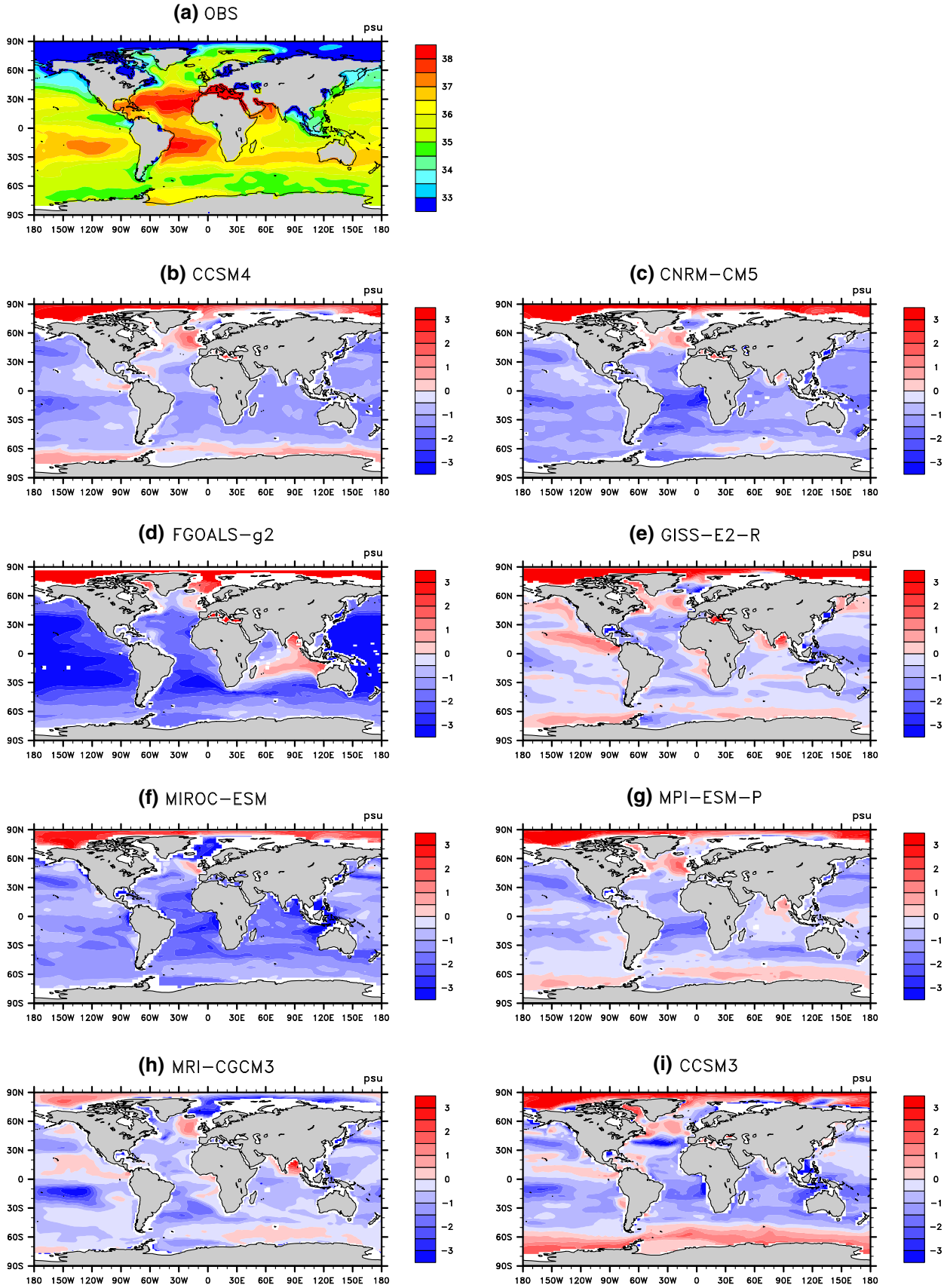
(a) OBS
psu
38
37
36
35
34
33
(b) CCSM4
(c) CNRM−CM5
(d) FGOALS−g2
(e) GISS−E2−R
(f) MIROC−ESM
(g) MPI−ESM−P
(h) MRI−CGCM3
(i) CCSM3
3
2
1
0
−1
−2
−3
90N
60N
30N
0
30S
60S
90S
180 150W 120W 90W 60W 30W 0 30E 60E 90E 120E 150E 180

AMOC induces a series of climate feedbacks which in turn act to stabilize the AMOC during the last deglaciation.

Two more issues merit further attentions on the feedback term. First, it is not clear whether above climate feedback in CCSM3 is a common feather occurring in all the CGCM simulations. This is because, even the bipolar seesaw response is generated in most CGCMs to the freshwater hosing in the North Atlantic (e.g., Stouffer et al. 2006; Kageyama et al. 2013), the wind response over the South Atlantic, however, has not been extensively studied in corresponding hosing experiments. Second, the feedback term may appear in different scenarios under different climates. Under the LGM climate, the increased Δs mainly results from the salinified surface and thermocline waters at 34°S. Whilst under the present day climate, the increase of Δs is mostly caused by the freshening in NADW (Liu et al. 2013).

4.3 The term related to the AABW cell $O(\mathcal{E}_{SO})$

The $O(\mathcal{E}_{SO})$ term is associated with changes in the deep cell strength and the deep ocean stratification, both of which are related to the formation of deglacial AABW. From 19.0 ka, due to a bipolar seesaw effect and a global CO_2-induced warming, a deglacial warming trend proceeds in the SH (Sachs et al. 2001) and leads to a large area of sea-ice melting around the Antarctica. The sea-ice melting contributes most of the change in buoyancy forcing and plays a dominant role in reducing the AABW formation as well as the deep cell strength (Liu 2012). Meanwhile, AABW is diluted by the sea-ice melting and the abyssal stratification weakens as well due to the AABW sinking and mixing in the deep ocean. As a result, M^{SO}_{ovS} in TraCE-21 appears as a decreased freshwater import from 19 ka to 17 ka, so $\partial\overline{M^{SO}_{ovS}}/\partial\overline{\psi} < 0$, suggesting that the deglacial AABW cell works on a freshwater accumulation in the Atlantic basin that helps to induce a bi-stable AMOC. Here, it is worth mentioning that variations in M^{SO}_{ovS} are not generated by directly changing the AMOC transport, but indirectly through a suite of ocean–atmosphere responses to the deglacial AMOC change.

Besides, we would like to point out that the $O(\mathcal{E}_{SO})$ term may vary greatly among CGCMs, due to the different abyssal stratifications and circulations. First, unlike CCSM3, some CMIP5/PMIP3 models (such as MPI-ESM-P) simulate a glacial abyssal stratification similar to the present day in which AABW is colder but fresher than NADW (Fig. 11b). In these models, the AABW cell will induce a freshwater import instead of a freshwater export at 34°S. Also, depending on the glacial sea-ice extent over the

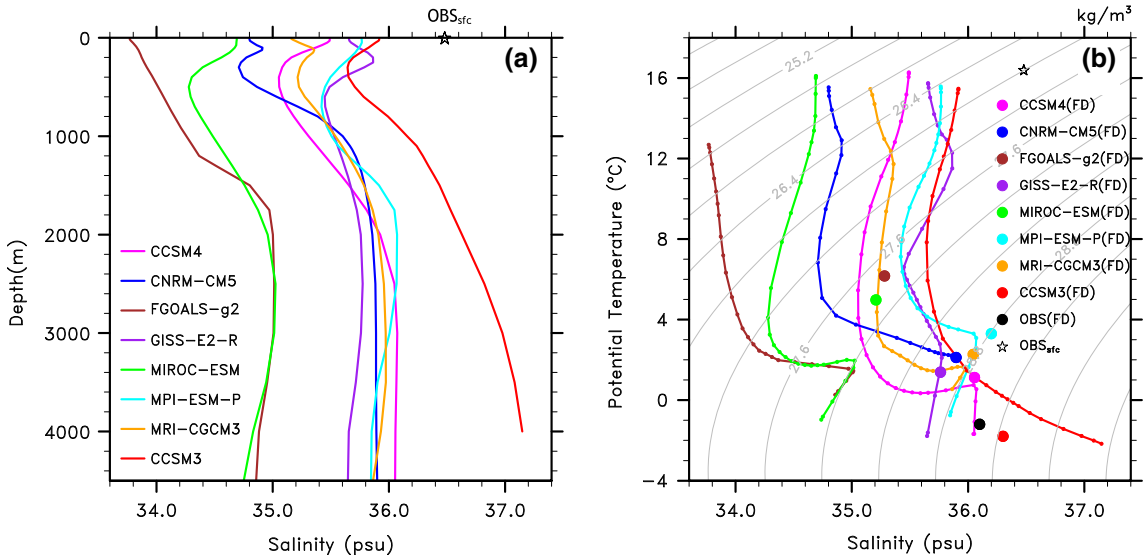

Fig. 11 **a** Vertical profiles of zonal mean salinity along 34°S at the LGM from seven CMIP5/PMIP3 CGCMs and CCSM3. Also, the zonal mean SSS along 34°S from a reconstructed dataset (Schäfer-Neth and Paul 2003) is shown as star. **b** Temperature and salinity diagram for models and observations. For models, it includes profiles of zonal mean temperature and salinity along 34°S at the LGM from seven CMIP5/PMIP3 CGCMs and CCSM3 (with the same color scheme with plot **a**). For observations, it includes the surface (*star*) and abyssal (*black dot*) values at the LGM. The surface observation is the zonal mean SST and SSS along 34°S, calculated from a reconstructed dataset (Schäfer-Neth and Paul 2003). The abyssal observation along 34°S is unavailable so far; hence we substitute an ODP data at the site 981, Feni Drift (55.48°N, 14.65°W; 2,184 m) in the North Atlantic (Adkins et al. 2002) by assuming the properties of NADW, as represent by the observation at Feni Drift, are conserved as the water mass reaching 34°S. Moreover, to evaluate the model bias in the simulation of NADW, we compare the model temperature and salinity from the most adjacent grid to Feni Drift (dots with colors corresponding to each CGCM) with the observation at Feni Drift. In the legend, all model results and observation at Feni Drift are labeled with "FD"

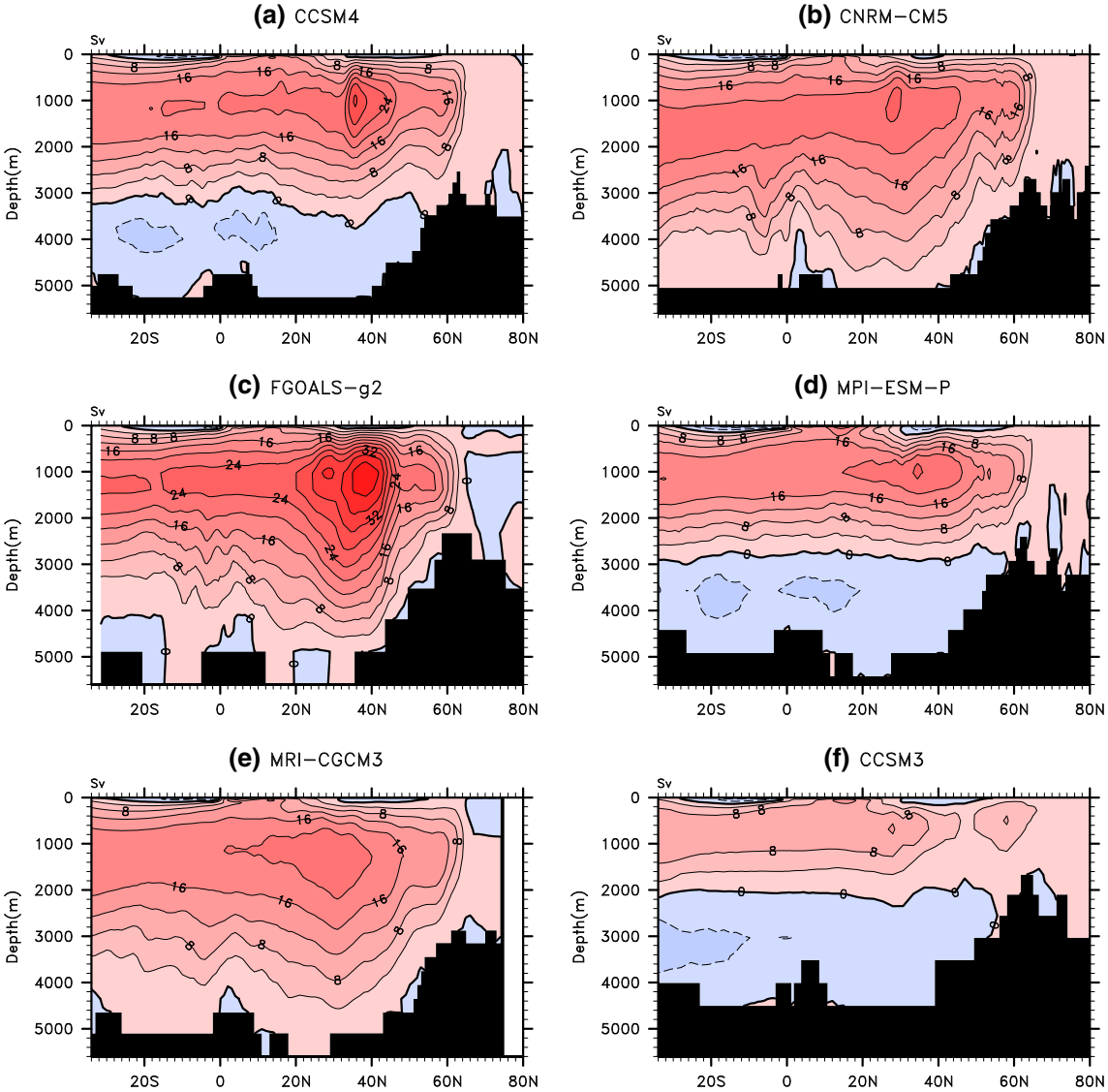

Fig. 12 Atlantic overturning streamfunction (*contoured* in Sv) in **a**–**e** CMIP5/PMIP3 CGCMs and **f** CCSM3, which is calculated as the mean over the whole period of each simulation (Table 1). For CCSM3, streamfunction is calculated at 21 ka in order to be consistent with CMIP5/PMIP3 models

Southern Ocean (Otto-Bliesner et al. 2007), some CMIP5/PMIP3 CGCMs may fail to simulate an AABW deep cell in their LGM climates. As shown in Fig. 12, AABW and its related deep cell almost disappear in CNRM-CM5, FGOALS-g2 and MRI-CMCM3.

4.4 The term from the northern boundary $O(\mathcal{E}_N)$

The term of $-\partial\overline{M_{ovN}}/\partial\overline{\psi}$ represents the effect from the Arctic on the AMOC stability. As described in Sect. 3.1, the only access for the freshwater exchange between the Arctic and the North Atlantic is through the Fram Strait prior to 13.1 ka. A weak freshwater export ($M_{ovN} > 0$) is primarily induced by an Atlantic outflow in the upper 600 m across the Fram Strait during the LGM (Liu et al. 2013), which slowly decreases to zero and switches to a weak freshwater import in late H1 (Fig. 2d). As a result, $-\partial\overline{M_{ovN}}/\partial\overline{\psi}$ is a small order term $O(\mathcal{E}_N)$ from the LGM to H1. However, during the BA, M_{ovN} increases and becomes comparable with M_{ovS} in magnitude after 14.0 ka (Fig. 2d). Therefore, the term of $-\partial\overline{M_{ovN}}/\partial\overline{\psi}$ is expected to become significant towards the early Holocene, especially when the BS opens and the climate gets more close to the modern state. A recent study (Liu et al. 2013) shows that, under the modern climate, the BS opening will enhance the freshwater exchange between the northern North Atlantic and the Arctic, via the Fram Strait, the CAA and the western shelf of the Barents Sea (in TraCE-21, the CAA is opened

in mid-Holocene and the Barents Sea is opened in Younger Dryas), and therefore modulate the stability of the AMOC.

5 Conclusions and discussions

In this study, we examine the AMOC stability during the last deglaciation based on a transient simulation by the NCAR CCSM3. Corresponding to an AMOC shutdown (from the LGM to H1) and later resumption (from H1 to the BA), an anomalous freshwater divergence and later convergence are induced by the AMOC in the Atlantic basin, which indicates a negative basin-scale salinity advection feedback and a mono-stable AMOC during the early stage of the last deglaciation. This anomalous Atlantic freshwater divergence or convergence is mostly contributed by variations in the freshwater transport (M_{ovS}) across 34°S. From 19 to 17 ka, M_{ovS} switches from a freshwater import to a freshwater export, which is mainly caused by two factors with about equal contributions, a reduced northward flow and a salinity increase in the surface and thermocline waters. The former factor results from the collapse of the AMOC, yet the latter factor is caused by a mechanism associated with climate feedbacks by the deglacial AMOC. More specifically, the cessation of the LGM AMOC in H1 causes a bipolar seesaw response as presents a SST warming (cooling) in the South (North) Atlantic. Meanwhile, surface winds are weakened over the tropical South Atlantic by a rationale analogy to the AMM but little affected in the subtropical South Atlantic. As a result, evaporation enhances over 20–44°S due to a warmer SST, which leads to a salinity increase in the surface and thermocline (via subduction of the SASTMW) waters at 34°S. Besides, the riverine discharge diminishes from the Sanaga and Nyong Rivers as well as the Congo River, probably due to the regional change in precipitation over the equatorial western Africa. This reduced runoff produces anomalously salty water near the estuary that is carried by the ocean currents, contributing to the salinification in the upper ocean at 34°S.

Several intriguing implications are presented on the paleoclimate simulations by CGCMs. The decomposition of a stability indicator L shows that the AMOC stability, in the early stage of the last deglaciation, is largely determined by two terms: the salinity stratification at 34°S and the change of stratification with the AMOC. Both terms are positive in TraCE-21, suggesting a negative basin-scale salinity advection feedback and a mono-stable AMOC. However, the former term is likely to be a biased model result in most CGCMs, primarily by the negative salinity bias in the surface and thermocline waters. As a result, the AMOC from the CGCM simulations is potentially subject to a bias of mono-stability.

In the following, we will discuss several related issues. First, the reconstructed salinity data from proxy records suggests that the surface water is salter than underlying NADW at 34°S; as such the realistic stratification term should be negative during the LGM. Thereupon L is likely negative in case of a combination between a strongly negative stratification term and a weakly positive feedback term, which then indicates a potential bi-stable LGM AMOC in reality. In another word, by correcting the salinity bias in the upper ocean at 34°S, we will be able to tune the model to simulate a bi-stable glacial AMOC. This will further imply a totally different scenario in the deglacial simulation by CGCMs, especially with regards to the scheme of MWF. Here, a similar case of this issue has been examined in Liu et al. (2014) under the modern climate. In the paper, they showed a negative surface salinity bias in the South Atlantic in several CGCMs (including CCSM3; c.f. Large and Danabasoglu 2006 for more details of upper ocean bias in CCSM3) due to a commonly existing double ITCZ problem. However, they further showed that, by using a surface flux adjustment, this salinity bias could be corrected, which leads to a bi-stable AMOC as is thought to be more close to the realistic case in the modern climate. In a word, the work of Liu et al. (2014) set a benchmark for further studies of glacial AMOC stability as related to the model bias correction.

Second, we would like to clarify that mechanism of the feedback term is primarily driven by the MWF instead of other forcings, which is demonstrated by a sensitivity experiment (HYS) in which the effects of orbital parameters, GHGs, continental ice-sheet, irregularity of MWF scheme are excluded. In particular, we make a parallel analysis between HYS and DGL-A in Figs. 6, 7 and 8, and results from HYS are highly similar to those in DGL-A. Moreover, the AMOC exhibits a general linear response to MWF in either of hysteresis diagrams, the diagram for HYS (c.f. Fig. 1e in Liu et al. 2013) and the diagram for TraCE-21 (Fig. 3a). However, if we observe and compare two diagrams carefully, we will find that the AMOC response in HYS is more close to linear. In TraCE-21 (Fig. 3a), there is an insignificant hysteresis loop between MWFs of 0.1 and 0.23 Sv, which is probably related to the deglacial changes in orbital parameters, GHGs and continental ice-sheet.

Third, it is worth noting that, accompanying with the collapse of glacial AMOC from the LGM to H1, a substantial reduction is expected in the AMOC-induced heat transport, which tends to enhance the sea-ice coverage in the northern North Atlantic, inhibit the NADW formation there by reducing the heat loss to the atmosphere and providing additional surface water, and finally slow down the recovery of the AMOC. This is a feedback related to the glacial sea-ice response, as described in Bitz et al.

(2007). We do not include the sea-ice feedback in this paper, but would like to leave it for future studies.

The final issue is about an uncertain factor in the stratification term, i.e., Agulhas leakage, the transport of warm and salty Indian Ocean waters into the Atlantic Ocean (e.g., Gordon et al. 1992; De Ruijter et al. 1999; Lutjeharms 2006). From paleo-proxy data, the amount of Agulhas leakage is subject to substantial glacial-to-interglacial variations (e.g., Biastoch et al. 2009; Beal et al. 2011; De Deckker et al. 2012). An increased (decreased) leakage contributes to a salinification (freshening) of the South Atlantic thermocline water, thereby modulates the stratification at 34°S and thus the AMOC stability. So it is a nontrivial task to correctly simulate Agulhas leakage by well resolving nonlinear dynamics (inertial mechanisms and ring formation) associated with Agulhas leakage. In particular, an effective resolution of at least 0.1° is needed for simulating Agulhas retroflection by inertial choking (Biastoch et al. 2009; Tsugawa and Hasumi 2010). However, as seen from Table 1, most CMIP5/PMIP3 have coarse resolution of $\sim 1°$ (CCSM4 has a finer resolution but still not enough), with large eddy viscosity in the ocean component, and upon that Agulhas retroflection is generated in these models via 'viscous choking' instead of inertial choking. This will lead to something wrong in amplitudes of Agulhas transport and leakage and their sensitivity to deglacial changes. Therefore, it would be desirable to resolve this problem in the future paleoclimate simulations.

Acknowledgments Wei Liu and Zhengyu Liu are supported by NSF, DOE and NSFC 41,130,105. Jun Cheng is supported by NSFC 41206024. Haibo Hu is supported by the National Key Program for Developing Basic Science (Grant Nos. 2010CB428504, 2012CB956002).

References

Adegbie AT, Schneider RR, Rohl U, Wefer G (2003) Glacial millennial scale fluctuations in central African precipitation recorded in terrigenous sediment supply and freshwater signals offshore Cameroon. Palaeogeogr Palaeoclimatol Palaeoecol 197:323–333

Adkins JF, McIntyre K, Schrag DP (2002) The salinity, temperature, and δ18O of the glacial deep ocean. Science 298:1769–1773

Alley RB (2000) The Younger Dryas cold interval as viewed from central Greenland. Quat Sci Rev 19(1–5):213–226. doi:10.1016/S0277-3791(99)00062-1

Barker S, Diz P, Vautravers MJ, Pike J, Knorr G, Hall IR, Broecker WS (2009) Interhemispheric Atlantic seesaw response during the last deglaciation. Nature 457:1097–1102

Beal LM, De Ruijter WPM, Biastoch A, Zahn R, SCOR/WCRP/IAPSO Working Group 136 (2011) On the role of the Aguhlas system in ocean circulation and Climate. Nature 472:429–436

Biastoch A, Böning CW, Schwarzkopf FU, Lutjeharms JRE (2009) Increase in Agulhas leakage due to poleward shift of Southern Hemisphere westerlies. Nature 462:495–499

Bitz CM, Chiang JCH, Cheng W, Barsugli JJ (2007) Rates of thermohaline recovery from freshwater pulses in modern, Last Glacial Maximum, and greenhouse warming climates. Geophys Res Lett 34:L07708. doi:10.1029/2006GL029237

Blunier T, Brook EJ (2001) Timing of millennial-scale climate change in Antarctica and Greenland during the last glacial period. Science 291:109–112

Boyle EA, Keigwin LD (1987) North Atlantic thermohaline circulation during the last 20,000 years: link to high latitude surface temperature. Nature 330:35–40

Bryan F (1986) High-latitude salinity effects and interhemispheric thermohaline circulations. Nature 323:301–304

Carlson AE (2009) Geochemical constraints on the Laurentide Ice Sheet contribution to Meltwater Pulse 1A. Quat Sci Rev 28:1625–1630. doi:10.1016/j.quascirev.2009.02.011

Chang P, Ji L, Li H (1997) A decadal climate variation in the tropical Atlantic ocean from thermodynamic air–sea interactions. Nature 385:516–518

Chiang JCH, Vimont DJ (2004) Analogous Pacific and Atlantic meridional modes of tropical atmosphere–ocean variability. J Clim 17:4143–4158

Cimatoribus AA, Drijfhout SS, den Toom M, Dijkstra HA (2012) Sensitivity of the Atlantic meridional overturning circulation to south Atlantic freshwater anomalies. Clim Dyn 39:2291–2306

Clark PU, Mix AC (2002) Ice sheets and sea level of the Last Glacial Maximum. Quat Sci Rev 21(1–3):1–7

Clark PU, Marshall SJ, Clarke GKC, Hostetler SW, Licciardi JM, Teller JT (2001) Freshwater forcing of abrupt climate change during the last glaciation. Science 293(5528):283–287. doi:10.1126/science.1062517

Clark PU, Mitrovica JX, Milne GA, Tamisiea ME (2002) Sea-level fingerprinting as a direct test for the source of global meltwater pulse IA. Science 295(5564):2438–2441. doi:10.1126/science.1068797

Collins WD, Bitz CM, Blackmon ML, Bonan GB, Bretherton CS, Carton JA, Chang P, Doney SC, Hack JJ, Henderson TB, Kiehl JT, Large WG, McKenna DS, Santer BD, Smith RD (2006) The community climate system model: CCSM3. J Clim 19:2122–2143

Cuffey KM, Clow GD (1997) Temperature, accumulation, and ice sheet elevation in central Greenland through the last deglacial transition. J Geophys Res 102(C12):26383–26396

Dansgaard W, Johnsen SJ, Clausen HB, Dahl-Jensen D, Gundestrup NS, Hammer CU, Hvidberg CS, Steffensen JP, Sveinbjörnsdottir AE, Bond G (1993) Evidence for general instability of past climate from a 250-kyr ice-core record. Nature 364(6434):218–220

De Deckker P, Moros M, Perner K, Jansen E (2012) Influence of the tropics and southern westerlies on glacial interhemispheric asymmetry. Nat Geosci 5(4):266–269

De Ruijter WPM, Biastoch A, Drijfhout SS, Lutjeharms JRE, Matano RP, Pichevin T, van Leeuwen PJ, Weijer W (1999) Indian–Atlantic inter-ocean exchange: dynamics, estimation, and impact. J Geophys Res 104:20885–20910

Dijkstra H (2007) Characterization of the multiple equilibria regime in a global ocean model. Tellus 59A:695–705

Dong B, Sutton RT (2002) Adjustment of the coupled ocean–atmosphere system to a sudden change in the thermohaline circulation. Geophys Res Lett 29. doi:10.1029/2002GL015229

Donners J, Drijfhout SS, Hazeleger W (2005) Water mass transformation and subduction in the South Atlantic. J Phys Oceanogr 35:1841–1860

Drijfhout SS, Weber SL, van der Swaluw E (2011) The stability of the MOC as diagnosed from model projections for pre-industrial, present and future climates. Clim Dyn 37:1575–1586. doi:10.1007/s00382-010-0930-z

Gordon AL, Weiss RF, Smethie WM, Warner MJ (1992) Thermocline and intermediate water communication between the South Atlantic and Indian Oceans. J Geophys Res 97:7223–7240

Heinrich H (1988) Origin and consequences of cyclic ice rafting in the northeast Atlantic Ocean during the past 130,000 years. Quat Res 29:142–152

Hu A, Meehl GA, Han W (2007) Role of the Bering Strait in the thermohaline circulation and abrupt climate change. Geophys Res Lett 34:L05704. doi:10.1029/2006GL028906

Hu A, Otto-Bliesner BL, Meehl GA, Han W, Morrill C, Brady EC, Briegleb B (2008) Response of thermohaline circulation to freshwater forcing under present day and LGM conditions. J Clim 21:2239–2258

Hu A, Meehl GA, Otto-Bliesner BL, Waelbroeck C, Han W, Loutre M, Lambeck K, Mitrovica J, Rosenbloom N (2010) Influence of Bering Strait flow and North Atlantic circulation on glacial sea level changes. Nat Geosci 3:118–121. doi:10.1038/NGEO729

Hu A, Meehl GA, Han W, Timmermann A, Otto-Bliesner BL, Liu Z, Washington W, Large W, Abe-Ouchi A, Kimoto M, Lambeck K, Wu B (2012) Role of the Bering Strait on the hysteresis of the ocean conveyor belt circulation and glacial climate stability. Proc Natl Acad Sci 109(17):6417–6422. doi:10.1073/pnas.1116014109

Huisman SE, den Toom M, Dijkstra HA, Drijfhout S (2010) An indicator of the multiple equilibria regime of the Atlantic meridional overturning circulation. J Phys Oceanogr 40:551–567. doi:10.1175/2009JPO4215.1

Jackson LC (2013) Shutdown and recovery of the AMOC in a coupled global climate model: the role of the advective feedback. Geophys Res Lett 40:1182–1188. doi:10.1002/grl.50289

Joos F, Spahni R (2008) Rates of change in natural and anthropogenic radiative forcing over the past 20,000 years. Proc Natl Acad Sci 105(5):1425–1430. doi:10.1073/pnas.0707386105

Kageyama M, Merkel U, Otto-Bliesner BL, Prange M, Abe-Ouchi A, Lohmann G, Roche DM, Singarayer J, Swingedouw D, Zhang X (2013) Climatic impacts of fresh water hosing under Last Glacial Maximum conditions: a multi-model study. Clim Past 9(2):935–953

Krebs U, Timmermann A (2007) Tropical air–sea interactions accelerate the recovery of the Atlantic meridional overturning circulation after a major shutdown. J Clim 20:4940–4956

Large WG, Danabasoglu G (2006) Attribution and impacts of upper-ocean biases in CCSM3. J Clim 19:2325–2346

Liu W (2012) Insights from deglacial changes in the Southern Ocean and Atlantic meridional overturning circulation during the last deglaciation. Ph.D thesis 150 pp. Univ of Wisconsin-Madison

Liu W, Liu Z (2013) A diagnostic indicator of the stability of the Atlantic meridional overturning circulation in CCSM3. J Clim 26:1926–1938

Liu W, Liu Z (2014) A note on the stability indicator of Atlantic meridional overturning circulation. J Clim 27:969–975

Liu Z, Otto-Bliesner BL, He F, Brady EC, Tomas R, Clark PU, Carlson AE, Lynch-Stieglitz J, Curry W, Brook E, Erickson D, Jacob R, Kutzbach J, Cheng J (2009) Transient simulation of last deglaciation with a new mechanism for Bølling–Allerød warming. Science 325:310–314

Liu W, Liu Z, Hu A (2013) The stability of an evolving Atlantic meridional overturning circulation. Geophys Res Lett 40:1562–1568. doi:10.1002/grl.50365

Liu W, Liu Z, Brady EC (2014) Why is the AMOC mono-stable in coupled general circulation models? J Clim 27:2427–2443

Lutjeharms JRE (2006) The agulhas current. Springer, Berlin

Lynch-Stieglitz J, Adkins JF, Curry WB, Dokken T, Hall IR, Herguera JC, Hirschi J, Ivanova E, Kissell C, Marchal O, Marchitto TM, McCave IN, McManus JF, Mulitza S, Ninnemann US, Yu E, Zahn R (2007) Atlantic overturning circulation during the Last Glacial Maximum. Science 316:66–69

Manabe S, Stouffer R (1988) Two stable equilibria of a coupled ocean–atmosphere model. J Clim 1:841–866

McManus JF, Francois R, Gherardi JM, Keigwin LD, Brown-Leger S (2004) Collapse and rapid resumption of Atlantic meridional circulation linked to deglacial climate changes. Nature 428(6985):834–837

Otto-Bliesner BL, Brady EC, Clauzet G, Tomas R, Levis S, Kothavala Z (2006) Last glacial maximum and Holocene climate in CCSM3. J Clim 19:2526–2544

Otto-Bliesner BL, Hewitt CD, Marchitto TM Jr, Brady EC, Abe-Ouchi A, Crucific M, Murakami S, Weber SL (2007) Last Glacial Maximum ocean thermohaline circulation: PMIP2 model intercomparisons and data constraints. Geophys Res Lett 34:L12707. doi:10.1029/2007GL029475

Peltier WR (2004) Global glacial isostasy and the surface of the ice-age Earth—the ICE-5G(VM 2) model and GRACE. Annu Rev Earth Planet Sci 32(1):111–149

Praetorius SK, McManus JF, Oppo DW, Curry WB (2008) Episodic reductions in bottom water currents since the last ice age. Nat Geosci 1:449–452

Provost C, Escoffier C, Maamaatuaiahutapu K, Kartavtseff A, Garcon V (1999) Subtropical mode waters in the South Atlantic Ocean. J Geophys Res 104:21033–21049

Rahmstorf S (1996) On the freshwater forcing and transport of the Atlantic thermohaline circulation. Clim Dyn 12:799–811

Rahmstorf S, Crucifix M, Ganopolski A, Goosse H, Kamenkovich IV, Knutti R, Lohmann G, Marsh R, Mysak LA, Wang Z, Weaver AJ (2005) Thermohaline circulation hysteresis: a model intercomparison. Geophys Res Lett 32:L23605. doi:10.1029/2005GL023655

Sachs JP, Anderson RF, Lehman SJ (2001) Glacial surface temperatures of the southeast Atlantic Ocean. Science 293:2077–2079

Schäfer-Neth C, Paul A (2003) The Atlantic Ocean at the last glacial maximum: 1. objective mapping of the GLAMAP sea-surface conditions. In: Wefer G, Mulitza S, Ratmeyer V (eds) The South Atlantic in the late quaternary: material budget and current systems. Springer, Berlin, pp 531–548

Shakun JD, Clark PU, He F, Marcott SA, Mix AC, Liu Z, Otto-Bliesner BL, Schmittner A, Bard E (2012) Global warming preceded by increasing carbon dioxide concentrations during the last deglaciation. Nature 484:49–54

Sijp WP (2012) Characterising meridional overturning bistability using a minimal set of state variables. Clim Dyn 39:2127–2142

Sijp WP, England MH, Gregory JM (2012) Precise calculations of the existence of multiple AMOC equilibria in coupled climate models. Part I: equilibrium states. J Clim 25:282–298

Stanford JD, Rohling EJ, Hunter SE, Roberts AP, Rasmussen SO, Bard E, McManus J, Fairbanks RG (2006) Timing of meltwater pulse 1a and climate responses to meltwater injections. Paleoceanography 21(4):PA4103

Stommel H (1961) Thermohaline convection with two stable regimes of flow. Tellus 2:224–230

Stouffer RJ, Dixon KW, Spelman MJ, Hurlin WJ, Yin J, Gregory JM, Weaver AJ, Eby M, Flato GM, Robitaille DY, Hasumi H, Oka A, Hu A, Jungclaus JH, Kamenkovich IV, Levermann A, Montoya M, Murakami S, Nawrath S, Peltier WR, Vettoretti G, Sokolov AP, Weber SL (2006) Investigating the causes of the response of the thermohaline circulation to past and future climate changes. J Clim 19:1365–1387. doi:10.1175/JCLI3689.11

Talley LD (2008) Freshwater transport estimates and the global overturning circulation: shallow, deep and throughflow components. Prog Oceanogr 78:257–303. doi:10.1016/j.pocean.2008.05.001

Taylor KE, Stouffer RJ, Meehl GA (2012) An overview of CMIP5 and the experiment design. Bull Am Meteorol Soc 93:485–498

Tsugawa M, Hasumi H (2010) Generation and growth mechanism of a Natal Pulse. J Phys Oceanogr 40:1597–1612

Weber SL, Drijfhout SS (2007) Stability of the Atlantic meridional overturning circulation in the last glacial maximum climate. Geophys Res Lett 34:L22706. doi:10.1029/2007GL031437

Weber SL, Drijfhout SS, Abe-Ouchi A, Crucifix M, Eby M, Ganopolski A, Murakami S, Otto-Bliesner BL, Peltier WR (2007) The modern and glacial overturning circulation in the Atlantic Ocean in PMIP coupled model simulations. Clim Past 3:51–64

Weldeab S, Schneider RR, Kölling M, Wefer G (2005) Holocene African droughts relate to eastern equatorial Atlantic cooling. Geology 33:981–984. doi:10.1130/G21874.1

Wu L, Li C, Yang C, Xie S-P (2008) Global teleconnections in response to a shutdown of the Atlantic meridional overturning circulation. J Clim 21:3002–3019

Xie S-P (1996) Westward propagation of latitudinal asymmetry in a coupled ocean–atmosphere model. J Atmos Sci 53:3236–3250

Xie S-P, Carton JA (2004) Tropical Atlantic variability: patterns, mechanisms, and impacts, in Earth's climate: the ocean–atmosphere interaction. Geophys Monogr Ser, vol 147, edited by Wang C, Xie S-P, Carton JA, AGU, Washington, DC, pp 121–142

Xie S-P, Philander SGH (1994) A coupled ocean–atmosphere model of relevance to the ITCZ in the eastern Pacific. Tellus(A) 46:340–350

Yeager S, Shields C, Large W, Hack J (2006) The low-resolution CCSM3. J Clim 19:2545–2566

Zhang R, Delworth T (2005) Simulated tropical response to a substantial weakening of the Atlantic thermohaline circulation. J Clim 18:1853–1860